J. Fluid Mech. (1989), *vol.* 209, *pp.* 77–92
Printed in Great Britain

Inviscid drops with internal circulation

By C. POZRIKIDIS

Department of Applied Mechanics and Engineering Sciences, R-011,
University of California at San Diego, La Jolla, CA 92093, USA

(Received 12 September 1988 and in revised form 9 May 1989)

The shape of a moving inviscid axisymmetric drop is considered as a function of surface tension and of the intensity of the internal circulation. In a frame of reference moving with the drop, the drop is modelled as a region of diffused vorticity which is bounded by a vortex sheet, and is imbedded in streaming flow. First, an asymptotic analysis is performed for a slightly non-spherical drop whose circulation is very close to that required for the spherical shape. The results indicate that steady drop shapes may exist at all but a number of distinct values of the Weber number, the lowest two of which are 4.41 and 6.15. For highly deformed drops, the problem is formulated as an integral equation for the shape of the drop, and for the strength of the bounding vortex sheet. A numerical procedure is developed for solving this equation, and numerical calculations are performed for Weber numbers between 0 and 4.41. Limiting members in the computed family of solutions contain spherical drops, and inviscid bubbles with vanishing circulation. Computed new shapes include saucer-like shapes with a rounded main body and an elongated tip. The relationship between inviscid drops and drops moving at large Reynolds numbers is discussed.

1. Introduction

The mechanics of moving bubbles and drops has received considerable attention because of its importance in a variety of applications, but also, because of its significance as a fundamental problem in fluid mechanics (Harper 1972; Clift, Grace & Weber 1978; Harper 1982). One of the better studied aspects of the problem is concerned with the shape of bubbles and drops that move, under the action of gravity, in an infinite ambient fluid. As a bubble or drop starts moving, vorticity is generated along its surface, and subsequently diffuses both outward and inward into the bubble or drop. The inward diffusing vorticity causes the gradual onset of internal circulation. In the case of bubbles, the viscosity of the internal fluid is much smaller than that of the suspending fluid, so that the internal circulation has little effect on the shape of the bubble and the dynamics of the external flow. In the case of drops, however, the internal circulation is of appreciable dynamical significance, and its presence may not be overlooked. For drops, the external flow is coupled with the internal flow via the boundary conditions on the drop surface, producing an involved free-boundary problem. This coupling considerably complicates the implementation of theoretical and computational methods of analysis including boundary-layer theory, integral, finite difference, and finite element formulations. With the exception of a recent study by Dandy & Leal (1989), all previous numerical investigations of drops relied on the assumption of spherical shape, requiring strong surface tension (see Oliver & Chung 1987 and references therein). From an

experimental standpoint, there are serious difficulties in measuring or even visualizing the internal drop motion without disturbing the drop shape or altering the physical properties of the fluids. It is thus not surprising that bubbles have been studied much more extensively, and are much better understood than drops.

In this paper we are concerned with the shape of inviscid drops with internal circulation moving in an unbounded ambient fluid. The primary objective of our analysis is to describe a family of shapes which constitutes a plausible asymptotic limit of drops moving at very high Reynolds numbers. A second objective is to demonstrate explicitly the existence of and to examine the structure of families of axisymmetric regions of concentrated vorticity, viewed as a special class of Batchelor flows (Moore, Saffman & Tanveer 1988). Before discussing these objectives further, it is necessary to outline the main features of our model.

Following Batchelor (1956), we argue that at high Reynolds numbers, the flow in the exterior of a moving drop is essentially irrotational, whereas the flow in the interior of the drop is rotational with diffused vorticity. There is a viscous boundary layer along the drop surface and along the axis of motion, inside and behind the drop. The surface boundary layer is similar to that developing along a solid body rather than to that developing around a gas bubble or a spherical drop, in the sense that it is responsible for a finite fraction of the total viscous dissipation. In our inviscid flow model, we assume that the external flow is perfectly irrotational, whereas the internal flow is rotational with perfectly diffused vorticity. To simulate the surface boundary layer, we assume that the tangential component of the velocity undergoes a discontinuity across the drop surface. This amounts to a vortex sheet. The pressure also undergoes a discontinuity across the drop surface which is balanced by surface tension. Neglecting viscous effects renders the shape of the drop a function of two parameters, namely the surface tension, expressed by the Weber number W, and of the intensity of the internal circulation.

Addressing now the physical relevance of our inviscid model, we note that both the Weber number and the intensity of the internal circulation are free parameters that may be assigned arbitrary values. In reality, both of these parameters are functions of the drop size and shape, as well as of the viscosity and density of the drop and of the suspending fluid. We have already indicated that when the viscosity of the drop is very small, the internal circulation may be neglected, leaving W as a single parameter of the flow. Furthermore, in this case, W may be related to the drag coefficient which in turn, may be related to the bubble size and shape, and to the physical properties of the drop and ambient fluid. This may be done by equating the rate of working of the drag force acting on the bubble to the rate of viscous dissipation within the external irrotational flow. Unfortunately, a similar calculation is not possible in the case of drops, for the dissipation in the boundary layer surrounding a drop is of the same order as that within the external and internal flow. A boundary-layer analysis or numerical calculations at large Reynolds numbers are necessary to produce this information.

In our inviscid flow model we neglect the presence of wakes that may develop behind moving drops. Previous studies have shown that these wakes may take the form of standing toroidal vortices, or of trains of unsteadily shed eddies (Rivkind & Ryskin 1976; Clift *et al.* 1978, p. 184; Dandy & Leal 1989). There is evidence, however, that while these wakes affect the shape of the rear part of the drop, they have small influence on the shape of the front part of the drop (Ryskin & Leal 1984). Furthermore, it is not clear that these wakes persist at very high Reynolds numbers (Dandy & Leal 1986, 1989). In our inviscid model, we also neglect the presence of

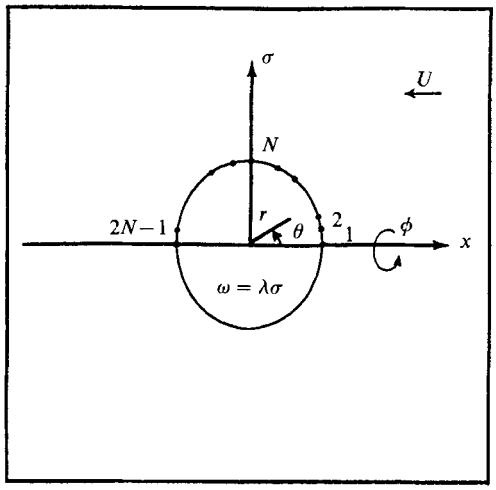

FIGURE 1. Schematic illustration of an axisymmetric drop placed in a uniform stream U.

gravitational forces in the dynamic balance along the drop surface. Strictly speaking, this approximation is valid when the drag coefficient c_d is small (Miksis, Vanden-Broeck & Keller 1982; El Sawi 1974). Previous numerical work, however, indicates that this may be a reasonable approximation even when c_d is of order one (Ryskin & Leal 1984; Dandy & Leal 1989). Neglecting gravitational forces is particularly convenient for our purposes, for it allows us to focus on the effect of the drop circulation, and to consider drop shapes with fore-and-aft symmetry.

To set up the grounds for our analysis, it is helpful to summarize previous results for spherical drops. In the context of inviscid flow theory, the flow outside an inviscid spherical drop is potential flow past a sphere, whereas the flow inside the drop is identical to that inside Hill's spherical vortex. The strength of the vorticity inside the drop may be arbitrary, and must be specified by physical considerations. A number of authors have chosen

$$\frac{\omega}{\sigma} = \frac{15}{2}\frac{U}{a^3}, \tag{1.1}$$

(Harper 1972) where U is the speed of the drop, a is the radius of the drop, ω is the azimuthal component of the vorticity, and σ is the distance from the axis of motion (figure 1). The choice (1.1) renders the velocity continuous across the surface of the drop, and hence, it prevents excessive viscous stresses associated with vortex sheets. Boundary-layer analysis shows that viscosity modifies the primary inviscid flow by introducing thin viscous layers along the surface of the drop and along the axis of motion, inside the behind the drop. These layers cause a reduction in the internal drop circulation by a factor that is proportional to the inverse square root of the Reynolds number $Re^{-\frac{1}{2}}$ (Harper & Moore 1968). Note that although (1.1) preserves the continuity of the velocity field, for $\alpha \neq 1$, it introduces discontinuities in the pressure across the drop surface. This causes drop deformation, and necessitates the action of surface tension to restore the spherical shape.

The rest of our paper is structured as follows. In §2 we present an asymptotic analysis valid for slightly non-spherical drops whose circulation is very close to that required for the spherical shape. The solution procedure employs the classical method of separation of variables. In §3 we formulate the problem as an integral equation, and develop a numerical method of solution. We then present numerical

results for highly deformed drops at low and moderate Weber numbers (high surface tension). In §4 we summarize and discuss the physical relevance of our results.

2. Asymptotic analysis for nearly spherical drops

We consider the steady motion of an inviscid, nearly spherical, axisymmetric drop. It is convenient to refer to a frame of reference moving with the drop, in which the drop is a stationary entity imbedded in a uniform stream with velocity U (figure 1). We refer to spherical polar coordinates (r, θ, ϕ) with corresponding velocity components (u, v, w), and introduce the Stokes streamfunction ψ defined by the equations

$$u = \frac{1}{r^2 \sin\theta} \frac{\partial \psi}{\partial \theta}, \tag{2.1a}$$

$$v = -\frac{1}{r \sin\theta} \frac{\partial \psi}{\partial r}. \tag{2.1b}$$

In terms of the stream function, the azimuthal component of the vorticity is equal to

$$\omega = \mathrm{D}^2 \psi \equiv -\frac{1}{r \sin\theta} \left[\frac{\partial^2 \psi}{\partial r^2} + \frac{\sin\theta}{r^2} \frac{\partial}{\partial \theta} \left(\frac{1}{\sin\theta} \frac{\partial \psi}{\partial \theta} \right) \right]. \tag{2.2}$$

At the outset, we non-dimensionalize all variables using as characteristic velocity the free-stream velocity U, and as characteristic length the equivalent drop radius $a = (3V/4\pi)^{\frac{1}{3}}$, where V is the drop volume. Assuming that the velocity field deviates only slightly from its basic state, corresponding to the spherical shape, we introduce asymptotic expansions for the streamfunction for both the interior and exterior flow

$$\hat{\psi} = \hat{\psi}_0 (1+\epsilon) + \epsilon \hat{\psi}_1 + O(\epsilon^2), \tag{2.3a}$$

$$\psi = \psi_0 + \epsilon \psi_1 + O(\epsilon^2), \tag{2.3b}$$

where ϵ is a small number compared to unity. A circumflex indicates variables in the interior of the drop. The streamfunction of the basic state is equal to

$$\hat{\psi}_0 = \tfrac{1}{10} \lambda (1 - r^2) r^2 \sin^2\theta, \tag{2.4a}$$

$$\psi_0 = \frac{1}{2} \left(1 - \frac{1}{r^3} \right) r^2 \sin^2\theta, \tag{2.4b}$$

where λ is a constant. The corresponding azimuthal vorticity is

$$\hat{\omega}_0 = \lambda r \sin\theta = \lambda \sigma, \tag{2.5a}$$

$$\omega_0 = 0. \tag{2.5b}$$

Equation (2.4a) expresses flow inside Hill's spherical vortex, whereas (2.4b) expresses irrotational flow past a sphere. Examining next Bernoulli's equation along the drop surface, we find that the choice

$$\lambda = \lambda_0 = -\frac{15}{2} \frac{1}{\alpha^{\frac{1}{3}}}, \tag{2.6}$$

renders the pressure continuous across the drop surface. Here, α is the ratio of the densities between the drop and the suspending fluid, $\alpha = \hat{\rho}/\rho$. For $\alpha \neq 1$, however, (2.6) introduces discontinuities in the tangential velocity across the drop surface. On the other hand, the choice

$$\lambda = \lambda_1 = -\tfrac{15}{2}, \tag{2.7}$$

preserves the continuity of the velocity field, but introduce discontinuities in the pressure across the drop surface. It is clear that (2.6) is the proper choice in the context of inviscid flow theory, and thus, it is adopted in our further analysis. Note however, that when α is very small, (2.6) yields an excessive internal circulation which appears to be unrealistic and in contrast to observations. This renders our perturbation analysis physically acceptable only in a restricted range of $\alpha < 1$.

The flow fields expressed by ψ_i and $\hat{\psi}_i$, $i = 1, 2, \ldots$ are assumed to be irrotational, and thus, the vorticity field corresponding to (2.3*a*, *b*) is given exactly by

$$\hat{\omega} = \lambda_0(1+\epsilon) r \sin\theta, \tag{2.8a}$$

$$\omega = 0. \tag{2.8b}$$

The parameter ϵ is now identified with the proportional deviation of the drop circulation from that required for a spherical shape.

Assuming next that the boundary of the drop exhibits slight deviations from the spherical shape that are commensurate with ϵ, we write

$$r = R = 1 + \epsilon h(\theta) + O(\epsilon^2). \tag{2.9}$$

Our task will be to compute the perturbation stream functions, and the shape function h, subject to two boundary conditions along the drop surface: (i) the velocity component normal to the boundary of the drop on both sides must vanish, and (ii) the jump in the pressure across the drop surface must be balanced by surface tension. The first condition may be expressed as

$$\hat{\psi}(r = R) = \psi(r = R) = 0, \tag{2.10}$$

while the second condition may be expressed as

$$\alpha \hat{\boldsymbol{u}} \cdot \hat{\boldsymbol{u}} - \boldsymbol{u} \cdot \boldsymbol{u} + \frac{4k}{W} = c, \tag{2.11}$$

evaluated at $r = R$. The Weber number, W, is defined as $W = 2a\rho U^2/T$, T is the surface tension, k is the total curvature of the drop, and c is a constant which is related to the curvature of the drop at front or rear stagnation point k_{st} by $c = 4k_{st}/W$. The shape of the drop is determined, possibly in a non-unique manner, by any three of the four parameters λ, α, c, and W, as well as by the perturbation variable ϵ.

Substituting the expansions (2.3*a*, *b*) and (2.9) into the kinematic condition (2.10), and collecting terms of order ϵ we find

$$h = \frac{5}{\lambda_0} \frac{1}{\sin^2\theta} \hat{\psi}_1(r = 1) = -\frac{2}{3} \frac{1}{\sin^2\theta} \psi_1(r = 1). \tag{2.12}$$

Furthermore, recalling that the perturbation flow is irrotational, we write

$$\mathrm{D}^2 \hat{\psi}_1 = \mathrm{D}^2 \psi_1 = 0, \tag{2.13}$$

where the operator D^2 was defined in (2.2). In spherical polar coordinates, the general non-singular solution to these equations is

$$\hat{\psi}_1 = \sin^2\theta \sum_{n=1}^{\infty} A_n r^{n+1} P'_n(\cos\theta), \tag{2.14}$$

$$\psi_1 = \sin^2\theta \sum_{n=1}^{\infty} B_n \frac{1}{r^n} P'_n(\cos\theta), \tag{2.15}$$

(Moffatt & Moore 1978). The even-order coefficients in both of these series must vanish due to the assumed fore-and-aft symmetry of the flow. Substituting (2.14) and (2.15) into (2.12), we find that the odd-order coefficients are related through

$$B_n = \alpha^{\frac{1}{2}} A_n. \tag{2.16}$$

Furthermore, (2.12) suggests the following expansion for the drop shape

$$h = -\frac{2}{3} \sum_{n=1}^{\infty} B_n P'_n(\cos\theta). \tag{2.17}$$

It will be convenient to expand h in an alternative series involving Legendre polynomials

$$h = \sum_{n=1}^{\infty} h_n P_n(\cos\theta), \tag{2.18}$$

where the odd-order coefficients vanish owing to symmetry. To relate the coefficients in (2.17) and (2.18), we use the identity

$$(2n+1) P_n = P'_{n-1} - P'_{n+1}, \tag{2.19}$$

and find

$$B_n = \frac{3}{2}\left(\frac{h_{n+1}}{2n+3} - \frac{h_{n-1}}{2n-1}\right). \tag{2.20}$$

To order ϵ, the mean curvature of the drop is given by

$$k = 2 + \epsilon \sum_{n=1}^{\infty} (n+2)(n-1) h_n P_n, \tag{2.21}$$

(Lamb 1932, p. 475). We are now in a position to complete the solution to the first-order problem. We substitute the expansions (2.14), (2.15), (2.17) and (2.21) into the dynamic condition (2.11), and use the identity

$$P'_n = \frac{n(n+1)}{2n+1} \frac{P_{n-1} - P_{n+1}}{\sin^2\theta}, \tag{2.22}$$

to replace the derivatives of Legendre polynomials with Legendre polynomials. We then collect coefficients multiplying Legendre polynomials of the same order, and finally, we use (2.20) to derive an infinite system of linear algebraic equations for the coefficients h_n

$$h_{n-3} \frac{9(n-4)(n-2)(n-1)}{(2n-3)(2n-5)} - h_{n-1}\left[\frac{9(n-4)(n-2)(n-1)}{(2n-3)(2n-1)} + \frac{9(n+1)n(n-2)}{(2n+1)(2n-1)} - \frac{4}{W}(n-2)(n+1)\right] + h_{n+1} \frac{9n(n+1)(n-2)}{(2n+1)(2n+3)} = 3\delta_{n3}, \tag{2.23}$$

$n = 3, 5, \ldots$. This system is completed by specifying that the volume of the drop is equal to $\frac{4}{3}\pi$, yielding $h_0 = 0$. It is worth noting that with the above non-dimensionalization, the coefficients of (2.23), are independent of the density ratio α.

The asymptotic solution of (2.23) in the limit of vanishing Weber numbers (large surface tension) may be readily found to be

$$h_n = \tfrac{3}{16} W \delta_{n2}. \tag{2.24}$$

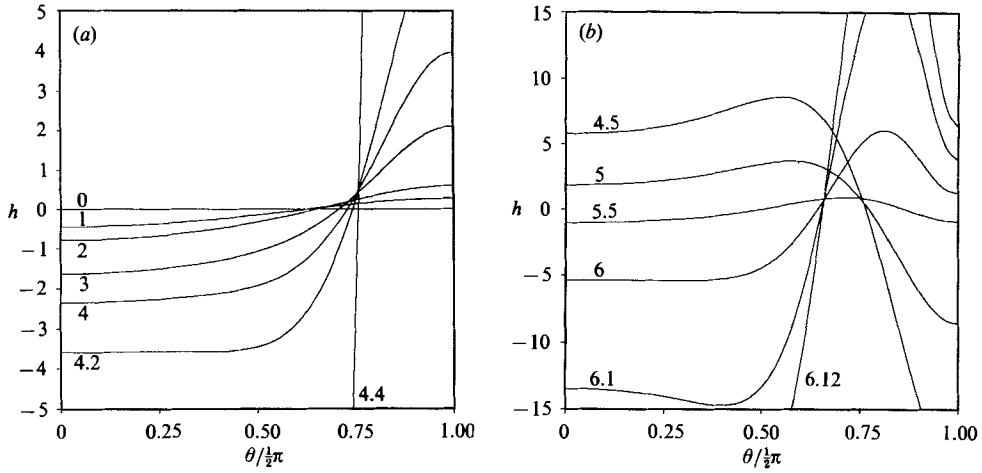

FIGURE 2. The deformation function $h(\theta)$ at several values of the Weber number. Note the singular behaviour at $W = 4.41$ and $W = 6.15$.

This shows that when surface tension is dominant, the drop takes the shape of an oblate spheroid, with the large axis normal to the direction of the flow. It is interesting to momentarily violate the assumption of small ϵ, and to set $\epsilon = -1$. In this manner, we recover an inviscid bubble with vanishing internal circulation whose boundary is described by the equation

$$r = 1 - \tfrac{3}{16} W P_2. \tag{2.25}$$

Comparison with the result of Moore (1959)

$$r = 1 - \tfrac{3}{32} W P_2, \tag{2.26}$$

pertaining to slightly distorted bubbles, indicates that our asymptotic analysis overestimates by a factor of two the drop deformation. This is due to the fact that in our perturbation expansion, the disturbance flows inside and outside the drop are assumed to be of the same order, while in the analysis of Moore (1959), the internal flow is by assumption equal to zero.

To compute the shape of the drop in the general case of finite W, we solve the infinite system (2.23) by truncation. In practice, we find that in the range of W considered, less than twenty terms are sufficient to produce results accurate to the third decimal place. Not surprisingly, we find that as W is increased, the boundary of the drop develops increasingly finer oscillations. In figure 2 (a, b) we plot the shape function $h(\theta)$ for several values of W. Examining figure 2 (a) we observe that for small values of W ($W = 1, 2, 3$), $h(\theta)$ is nearly a sinusoidal function, implying that the drop takes the shape of an oblate spheroid. At $W = 4$, we observe that the deformation of the drop becomes pronounced along the midplane $\theta = \frac{1}{2}\pi$, and then, at $W = 4.41$, we obtain a singular behaviour. At this value of W, the determinant of the system (2.23) changes sign independently of the level of truncation. As $W = 4.41$ is approached from lower or higher values, the drop develops a spike-like projection or depression at the midplane $\theta = \frac{1}{2}\pi$. In figure 2 (b) we plot $h(\theta)$ for values of W higher than 4.41. We observe oscillatory but regular behaviour until $W = 6.15$, where we encounter a second singular point. Further calculations showed the existence of a series of singular points at higher values of W. Thus, our asymptotic analysis indicates the

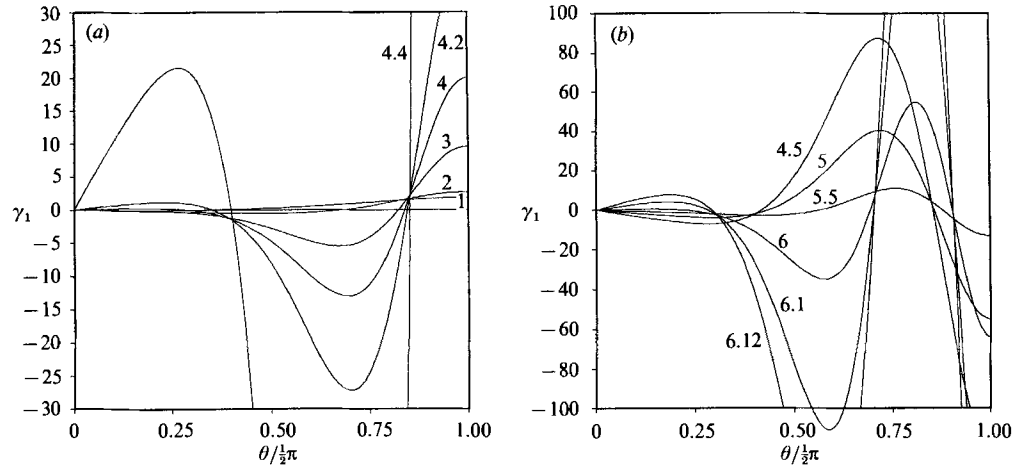

FIGURE 3. The strength of the modified surface vortex sheet $\gamma_1(\theta)$ at several values of the Weber number. Note the singular behaviour at $W = 4.41$ and $W = 6.15$.

existence of steady drop shapes at all but a number of distinct values of the Weber number.

To gain some insights into structure of the flow, we consider the strength of the vortex sheet residing along the drop surface. It is particularly instructive to subtract out the strength of the sheet corresponding to the undisturbed spherical shape, and to consider the strength of a modified vortex sheet, given by

$$\gamma = v - \alpha^{\frac{1}{2}}\hat{v} = -\epsilon\gamma_1 + O(\epsilon^2), \tag{2.27a}$$

$$\gamma_1 = \tfrac{3}{2} + 2\sum_{n=1}^{\infty} (n-2) B_n P'_n, \tag{2.27b}$$

(see also next section). Note that γ_1 is independent of the density ratio α. In figure 3(*a*, *b*) we plot γ_1 as a function of the polar angle θ for different values of W. We observe that the behaviour of γ_1 conforms with that of the shape function h, exhibiting a spike-like behaviour at the singular points $W = 4.41$ and $W = 6.15$.

The system (2.23) describes the shape of slightly non-spherical drops whose deformation is proportional to the deviation of the internal circulation from its unperturbed value. If we had stipulated that the circulation of the drop is undiminished, and yet, that the drop is slightly deformed, we would have found that the shape of the drop is described by the homogeneous system of (2.23). A non-trivial solution to this system is possible only at the singular points $W = 4.41, 6.15, \ldots$. This suggests that these points represent crossing points between distinct solution branches, a conjecture that will be validated in the next section. This behaviour is reminiscent of that of steady gravity–capillary waves on deep water (Chen & Saffman 1979, 1980).

3. Nonlinear analysis

3.1. *Formulation*

To compute the shape of highly non-spherical drops, we resort to numerical methods. Given the vorticity of the drop $\omega = \lambda\sigma$, we seek to calculate the shape of the drop, as well as the internal and external flow fields, subject to the kinematic condition

$$\boldsymbol{u}\cdot\hat{\boldsymbol{n}} = \hat{\boldsymbol{u}}\cdot\hat{\boldsymbol{n}} = 0, \tag{3.1}$$

and to the dynamic condition expressed by (2.11). Here, $\hat{\boldsymbol{n}}$ is the unit vector normal to the boundary of the drop. To make our formulation compact, we introduce the modified internal flow

$$\tilde{\boldsymbol{u}} = \alpha^{\frac{1}{3}}\hat{\boldsymbol{u}}, \tag{3.2a}$$

with azimuthal vorticity

$$\tilde{\omega} = \tilde{\lambda}\sigma, \tag{3.2b}$$

where

$$\tilde{\lambda} = \alpha^{\frac{1}{3}}\lambda. \tag{3.2c}$$

This modified flow must satisfy the kinematic boundary condition (3.1), and the dynamic condition

$$\tilde{\boldsymbol{u}}\cdot\tilde{\boldsymbol{u}} - \boldsymbol{u}\cdot\boldsymbol{u} + \frac{4k}{W} = c, \tag{3.3}$$

where k is the total curvature of the drop. Furthermore, it is convenient to decompose the modified internal flow as

$$\tilde{\boldsymbol{u}} = \tilde{\boldsymbol{u}}^{\mathrm{rot}} + \tilde{\boldsymbol{u}}^{\mathrm{pot}} + U\hat{\boldsymbol{i}}, \tag{3.4}$$

where $\tilde{\boldsymbol{u}}^{\mathrm{rot}}$ is a rotational flow field with vorticity (3.2b), and $\tilde{\boldsymbol{u}}^{\mathrm{pot}}$ is a potential flow field. We identify $\tilde{\boldsymbol{u}}^{\mathrm{rot}}$ with the flow induced by the vorticity distribution $\tilde{\omega}$, and $\tilde{\boldsymbol{u}}^{\mathrm{pot}}$ with the flow induced by a vortex sheet of strength γ residing along the drop surface. In this manner, we rewrite (3.4) in the form

$$\tilde{\boldsymbol{u}}(\boldsymbol{x}_0) = \int_A \boldsymbol{U}(x_0 - x, \sigma_0, \sigma)\,\tilde{\omega}\,\mathrm{d}S + \int_c \boldsymbol{U}(x_0 - x, \sigma_0, \sigma)\,\gamma\,\mathrm{d}l + U\hat{\boldsymbol{i}}, \tag{3.5}$$

where $\boldsymbol{U}$ is the fundamental flow induced by a vortex ring, and $\hat{\boldsymbol{i}}$ is the unit vector in the x-direction. The axial and radial components of $\boldsymbol{U}$ are given in Appendix A. Furthermore, we insist that (3.5) is valid in the exterior of the drop, as well as on the drop surface. In the second case, the second integral in (3.5) should be interpreted as a Cauchy principal value integral. The velocity expressed by (3.5) is discontinuous across the drop surface, and the limiting values of the velocity on either side of the surface are given by

$$\tilde{\boldsymbol{u}}^{(\pm)}(\boldsymbol{x}_0) = \tilde{\boldsymbol{u}}^{(0)}(\boldsymbol{x}_0) \pm \tfrac{1}{2}\gamma(\boldsymbol{x}_0)\,\hat{\boldsymbol{t}}, \tag{3.6}$$

where $\hat{\boldsymbol{t}}$ is the unit tangent vector, and the superscript zero indicates evaluation right on the drop surface. Using Stokes theorem, we may convert the area integral in (3.5) into a line integral over the drop contour (Pozrikidis 1986). This tranforms (3.5) into

$$\tilde{\boldsymbol{u}}(\boldsymbol{x}_0) = \int_c [\boldsymbol{U}(x_0 - x, \sigma_0, \sigma)\,\gamma + \tilde{\lambda}\boldsymbol{P}(x_0 - x, \sigma_0, \sigma)\hat{\boldsymbol{j}}\cdot\hat{\boldsymbol{t}}]\,\mathrm{d}l + U\hat{\boldsymbol{i}}, \tag{3.7}$$

where

$$P_x = \frac{\sigma}{4\pi}\Omega, \tag{3.8a}$$

$$P_\sigma = \frac{\sigma}{\sigma_0}G. \tag{3.8b}$$

Here, $\hat{\boldsymbol{j}}$ is the unit vector in the σ-direction, and Ω and G are the potential function and stream function associated with a vortex ring of unit strength. These may be expressed in terms of complete elliptic integrals of the first, second, and third kind as explained in Appendix A. In particular, Ω is equal to the solid angle subtended from the point (x_0, σ_0) to the ring (x, σ). Its consistent computation requires the introduction of a branch cut at $\sigma > \sigma_0$.

Substituting (3.6) into (3.1) and (3.3) we derive the boundary conditions

$$\tilde{\boldsymbol{u}}^{(0)} \cdot \hat{\boldsymbol{n}} = 0, \tag{3.9a}$$

and

$$\tilde{\boldsymbol{u}}^{(-)} \cdot \tilde{\boldsymbol{u}}^{(-)} - \tilde{\boldsymbol{u}}^{(+)} \cdot \tilde{\boldsymbol{u}}^{(+)} + \frac{4}{W}(k - k_{\rm st}) = 0. \tag{3.9b}$$

Given that the volume of the drop is equal to $\frac{4}{3}\pi$, and also, given $\tilde{\lambda}$, and W or $k_{\rm st}$, the problem is to solve (3.9a, b) for the strength of the sheet γ and for the drop shape.

3.2. *Numerical procedure*

In our numerical procedure we trace the boundary of the drop with $2N-1$ marker points, and approximate the shape of the drop with a collection of circular arcs passing through trios of successive points (figure 1). We assign to each point a value of the vorticity γ_i, and approximate the strength of the vortex sheet over each arc with a parabolic function with respect to arc length. In addition, we express the position of the marker points using a parametric representation. We have considered two such representations including $r(\theta)$, and $\{x(\sigma), \sigma(\theta) = \sigma(\frac{1}{2}\pi)\sin\theta\}$ with θ evenly spaced within $[0, \pi]$. Requiring that the drop is symmetric with respect to $x = 0$, we end up with $2N-1$ scalar unknowns including $\gamma_i, i = 2, \ldots, N$, and $r_i, i = 1, \ldots, N$ or $\sigma(\frac{1}{2}\pi)$, and $x_i, i = 1, \ldots, N-1$. We have acknowledged that $\gamma_1 = \sigma_1 = 0$.

To solve for the unknowns, we require a set of $2N-1$ equations. One equation comes from the restriction that the volume of the drop is equal to $\frac{4}{3}\pi$. $N-1$ additional equations arise by applying the dynamic condition (3.9b) at the points $i = 2, \ldots, N$. Finally, $N-1$ equations arise by applying the kinematic condition (3.9a) at the points $i = 1, \ldots, N-1$. In certain cases, we find it convenient, instead of specifying W, to specify a geometrical characteristic of the drop such as the curvature at the stagnation points $k_{\rm st}$ or the drop aspect ratio $\chi = \sigma(\theta = \frac{1}{2}\pi)/x(\theta = 0)$. In these cases, we treat W as an additional unknown, and supplement the above system with the imposed geometrical restriction. We solve the resulting system of equations by the method of Newton–Raphson. We evaluate all of the derivatives in the Jacobian matrix by numerical differentiation, except for the ones with respect to W. Furthermore, we exploit the fact that a change in the strength of the vortex sheet or in the position of a marker point produces changes only in the characteristics of the arcs that pass through this point to reduce the cost of the computation of the Jacobian. We compute the singular integrals of U and G in (3.7) by subtracting off, and then integrating analytically the singularities over each arc. The required regular numerical integrations are performed using the two-point Gauss–Legendre method.

Our numerical scheme is second-order accurate with respect to N. This was verified for slightly eccentric drops by the use of Richardson extrapolation. Unfortunately, increased computational cost has prevented us from performing calculations with a large number of points for highly deformed drops. All computations were performed with $N = 17$, and convergence was tested by comparing the results with those with $N = 13, 9, 5$, and with predictions of the asymptotic analysis. The results presented

in the next section have an error of less than 1%. The illustrated drop shapes are accurate within plotting accuracy.

To accelerate convergence we used continuation in our initial guesses. Furthermore, to reduce the cost of the computations, we updated the Jacobian matrix only once or twice during each run. In all cases, the calculations converged within five iterations. The major expense in our computations was the evaluation of the Jacobian matrix. For $N = 17$, each evaluation of the Jacobian required approximately 1.5 min of CPU time on the SDSC CRAY X-MP/4. A complete run required 3–4 min of CPU time.

3.3. *Results*

The asymptotic analysis of §2 revealed the existence of slightly deformed steady-drop shapes at all but a number of critical values of the Weber number. This suggested the existence of distinct branches of solutions extending between two successive critical values. In our numerical computations we confine our attention to the lowest branch $0 < W < 4.41$ for two reasons. First, high W yield oscillatory shapes that may not be resolved with sufficient accuracy in our numerical procedure. Second, experimental observations indicate that drop shapes at high W are unstable and hence, physically unrealizable (see discussion in the next section, but also note that in a quasi-steady approximation, the Weber number of a drop that accelerates from rest is continuously increasing, causing continuous deformation and destruction at the first critical point $W = 4.41$).

In our discussion we shall use the parameter λ', defined as

$$\lambda' = -\tfrac{2}{15}\tilde{\lambda} = -\tfrac{2}{15}\lambda\,\alpha^{\frac{1}{2}}. \tag{3.10}$$

Setting $\lambda' = 1$ (or $\lambda = \lambda_0$) yields spherical drops, whereas setting $\lambda' = 0$ yields bubbles with vanishing circulation.

In figure 4 (*a–c*) we present a representative compilation of computed drop shapes for $\lambda' = 0, 0.80, 0.950$, sorted in order of increasing aspect ratio χ. Before discussing these shapes, it is helpful to present an overall picture of our results by presenting a graph of the aspect ratio χ of a drop with respect to the Weber number (figure 5). As mentioned in the introduction, the case $\lambda' = 0$, was studied by several previous authors including Moore (1963, 1965), El Sawi (1974), and Miksis, Vanden-Broeck & Keller (1981). Our results are in perfect agreement with the numerical calculations presented by the last authors. The corresponding curve in figure 5 shows a mild maximum $W = 3.23$ at $\chi = 3.85$. This separates two solution branches, the one to the right, for the most eccentric shapes, probably being unstable. For $\lambda' = 0.40$, we observe behaviour very similar to that for $\lambda' = 0$, with the maximum W being virtually unchanged. This suggests that moderate internal circulation has minor influence on the drop shape. We note, however, that the aspect ratio corresponding to the maximum Weber number is appreciably shifted to lower eccentricities. For $\lambda' = 0.80$, we observe a distinct change in behaviour; the maximum W is well above the one for $\lambda' = 0$, whereas the eccentricity corresponding to this maximum is well below $\chi = 3.85$. The asymptotic behaviour as λ' tends to unity becomes evident by inspecting the curve for $\lambda' = 0.950$. This is characterized by a sharp increase at small eccentricities, a distinct maximum at $\chi \approx 1.3$, and a mild decrease at high eccentricities. At the end of the spectrum is the curve for $\lambda' = 1$. As suggested by the asymptotic analysis of §2, this curve crosses the $\chi = 1$ axis at the critical point $W = 4.41$.

We found that the shape of a drop with specified internal circulation may not be a unique function of the Weber number. As in the case of bubbles, we may speculate

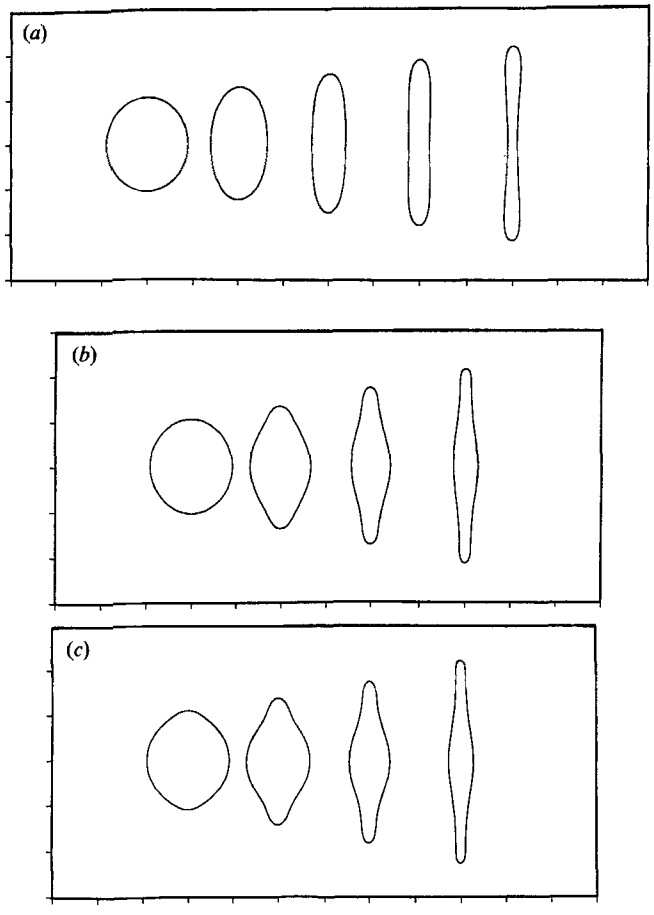

FIGURE 4. Drop shapes for three values of the circulation parameter $\lambda' = -\frac{2}{15}\lambda\alpha^{\frac{1}{2}}$, and for several values of the aspect ratio χ. (*a*) $\lambda' = 0$, $\chi = 1.016$, 2, 4, 8, 20; (*b*) $\lambda' = 0.80$, $\chi = 1.2$, 2, 4, 8.2; (*c*) $\lambda' = 0.95$, $\chi = 1.037$, 2, 4, 8. The corresponding Weber numbers may be deduced from figure 5.

that drops corresponding to the solution branches with the most eccentric shapes are unstable. If this is true, then increasing the drop circulation decreases the maximum possible aspect ratio for steady motion.

Let us now discuss the drop shapes shown in figure 4. Considering first the case of vanishing circulation (figure 4*a*), we observe that bubbles with low eccentricity resemble oblate spheroids, whereas bubbles with high eccentricity contain a dimple along the axis of motion. As χ is increased, the thickness of a bubble at the centreline tends to zero, and the bubble assumes the shape of a flattened ring (Miksis *et al.* 1981). The effect of internal circulation becomes evident by comparing these shapes to those shown in figure 4(*b*), for $\lambda' = 0.80$. In the second case, low χ drops resemble oblate spheroids, whereas high χ drops resemble saucers with a rounded main body and an elongated tip. These shapes bear a noticeable resemblance to those photographed by Winnikow & Chao (1966, see their figure 3(*e*, *g*, *k*)). The effect of drop circulation becomes more clear by inspecting figure 4(*c*), showing drop shapes with $\lambda' = 0.95$. For the most elongated shape shown in this picture, the segment connecting the main body to the tip of the drop is nearly vertical. Calculations

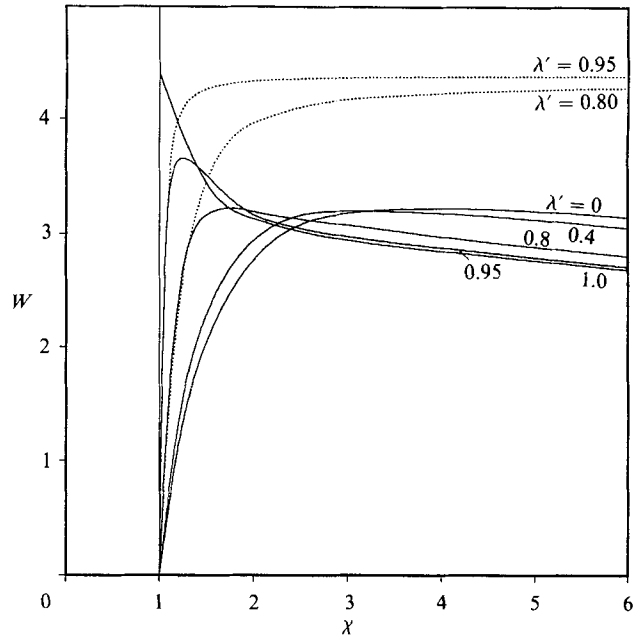

FIGURE 5. The Weber number as a function of the drop aspect ratio χ for several values of the internal circulation parameter λ'. The dotted lines represent asymptotic results for slightly non-spherical drops.

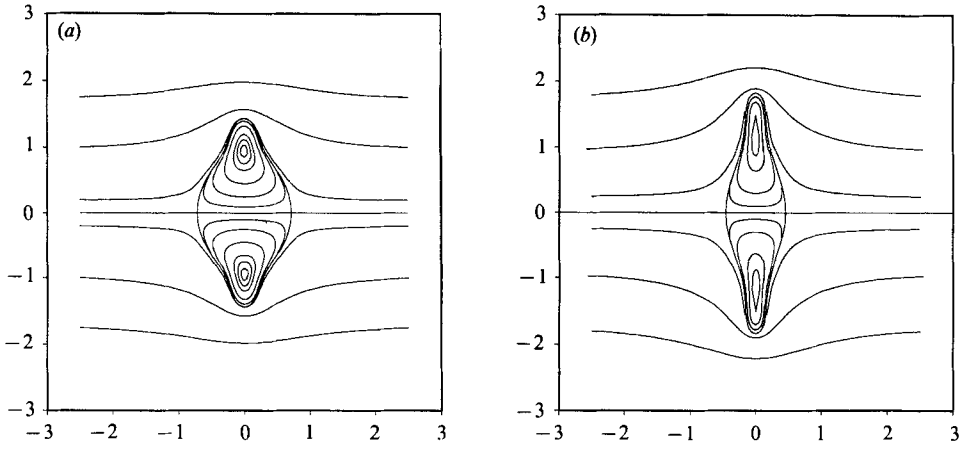

FIGURE 6. Streamline patterns for two drops with $\lambda' = 1.0$, and (*a*) $\chi = 2$, (*b*) $\chi = 4$.

beyond this point failed to converge. This was attributed to inadequate resolution of the crossing points between the branch cut of the solid angle Ω and the drop boundary. The results however, clearly indicated the formation of a dimple off the axis of motion, and suggested an asymptotic drop shape which is composed of a main central body and a secondary satellite ring. Overall, figure 4 suggests that increasing the internal drop circulation causes a corresponding increase in the thickness of the main body of a drop.

The structure of the flow inside and outside deformed drops is illustrated in figure 6(*a*, *b*) showing streamline patterns for two cases with $\lambda' = 1.0$, and $\chi = 2, 4$. In both

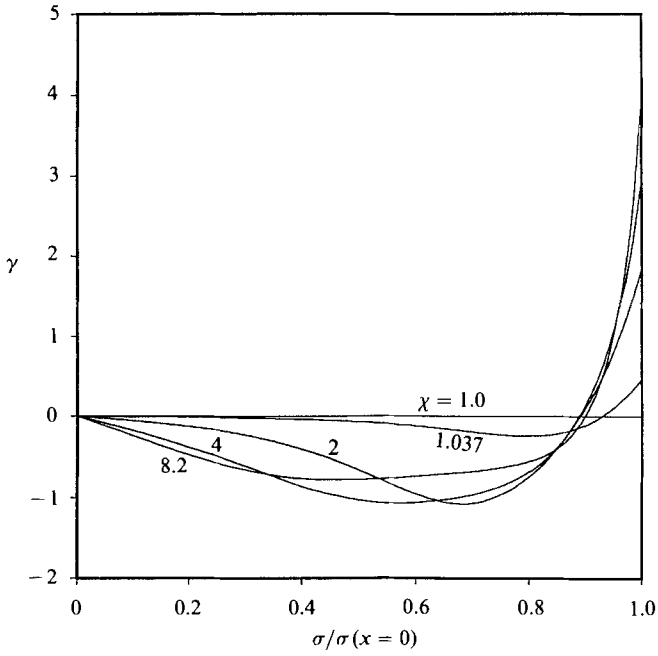

FIGURE 7. The strength of the modified bounding vortex sheet for $\lambda' = 0.95$, and several drop aspect ratios.

cases we observe that the centre of the internal vortex is outside the main body of the drop, suggesting an efficient recirculation of material elements inside the drop.

Finally, it is enlightening to consider the strength of the vortex sheet bounding the drop. This is plotted in figure 7 with respect to the radial position σ for $\lambda' = 0.95$, and for several values of χ. It is important to keep in mind that γ does not represent the actual discontinuity in the velocity across the boundary of the drop, except for the special case $\alpha = 1$. γ is a sinusoidal function of θ at small χ. Around the axis of motion and the tip of the drop, as χ is increased, γ increases in a corresponding monotonic fashion. In the intervening region, as χ is increased, γ increases, reaches a maximum, and then it decreases. This behaviour is attributed to the saucer-like drop shape, and reflects the presence of the main body and of the elongated tip.

4. Discussion

Experimental observations have shown that as the Reynolds number of a drop is increased, the drag coefficient decreases, reaches a minimum, and then, it increases at a fast rate. The Weber number corresponding to the minimum drag coefficient has an approximate value of 4, independent of the physical properties of the fluids (Harper 1972). More importantly, this characteristic Weber number separates two flow regimes with distinct behaviour. Drops at lower Weber numbers move steadily, whereas drops at higher Weber number execute oscillatory motions, break into smaller fragments, or develop skirts and dimples. One may remark that the above characteristic value of 4 is close to the first critical point $W = 4.41$. One is then tempted to speculate that unsteady drop motion may be linked to the non-existence of even slightly deformed drops at $W = 4.41$. There is of course the possibility that

drops become unstable owing to the development of unsteady wakes. A formal stability analysis is necessary to clarify the issue.

Experimental work with drops is limited to observations of drop shapes, visualization of the associated wakes and internal flow, and measurements of drag coefficients. To the author's knowledge, apart from the qualitative observation that increasing the drop deformation decreases the drop circulation, there is no published quantitative information on the intensity of the internal circulation. A comparison of our computations with experimental work must await further developments.

Recently, Dandy & Leal (1989) presented finite-difference calculations for deformable drops at low and intermediate Reynolds numbers. Their calculations are in good agreement with the analysis of Harper & Moore (1968) for moderate drop deformations and for α close to 1. Unfortunately, these authors do not present calculations for highly deformed shapes at sufficiently high Reynolds numbers, prohibiting a critical comparison with our results.

In summary, we have described a family of inviscid drops with internal motion, parametrized by the Weber number and the intensity of the internal circulation λ. We found that solutions may exist at all but a number of discrete values of the Weber number. Our calculated drop shapes include saucer-like shapes, with a rounded body and an elongated tip that bear close resemblance to shapes photographed by previous authors. We also found that increasing the drop circulation increases the thickness of the main body of a drop. We hope that our results will serve as a point of reference for future numerical work on drops at large Reynolds numbers.

I wish to thank Dr Scott Jones for reviewing the algebra in §2. Thanks are due to the Office of Academic Computing of UCSD for providing computer resources with the San Diego Supercomputer Center. Acknowledgement is made to the donors of The Petroleum Research Fund, administered by the ACS, for partial support of this research.

Appendix A

The axial and radial components of the velocity induced at the point $\boldsymbol{x}_0$, by a vortex ring of unit strength located at $\boldsymbol{x}$, are given by

$$U_x = -\frac{1}{2\pi\sigma_0}\left\{E(\alpha)\left[\frac{\sigma_0}{r_M}\frac{1+\alpha}{1-\alpha}-\frac{\sigma}{r_m}\frac{2}{1-\alpha}\right]-K(\alpha)\left[\frac{\sigma_0}{r_M}-\frac{\sigma}{r_m}\right]\right\},$$

$$U_\sigma = \frac{1}{2\pi\sigma_0}\frac{x_0-x}{r_M}\left(\frac{1+\alpha}{1-\alpha}E(\alpha)-K(\alpha)\right),$$

where

$$\alpha = \left[\frac{r_2-r_1}{r_2+r_1}\right]^2,$$

$$\frac{1}{r_M}=\frac{1}{r_1}+\frac{1}{r_2}, \quad \frac{1}{r_m}=\frac{1}{r_1}-\frac{1}{r_2}, \quad r_1^2=(x_0-x)^2+(\sigma_0-\sigma)^2, \quad r_2^2=(x_0-x)^2+(\sigma_0+\sigma)^2,$$

E and K are complete elliptic integrals of the first and second kind. The stream function associated with the vortex ring is given by (Lamb 1932)

$$G = \frac{1}{2\pi}(r_1+r_2)\,[K(\alpha)-E(\alpha)].$$

The solid angle subtended from the point $\boldsymbol{x}_0$ to the ring $\boldsymbol{x}$ is given by

$$\Omega = 2\pi \frac{x-x_0}{|x-x_0|} - \frac{1}{B} \frac{x-x_0}{((x-x_0)^2+(\sigma+\sigma_0)^2)^{\frac{1}{2}}} \{(C+1)\,\eta_1 \Pi(-\eta_1/k^2) - (C-1)\,\eta_2 \Pi(\eta_2/k^2)\}$$

where $$C = \frac{\sigma}{((x-x_0)^2+\sigma_0^2)^{\frac{1}{2}}}, \quad B = C\frac{\sigma_0}{\sigma}, \quad \eta_1 = \frac{2B}{1-B}, \quad \eta_2 = \frac{2B}{1+B},$$

and Π is the complete elliptic integral of the third kind (Pozrikidis 1986).

REFERENCES

Batchelor, G. K. 1956 On steady laminar flow with closed streamlines at large Reynolds number. *J. Fluid Mech.* **1**, 177–190.

Chen, B. & Saffman, P. G. 1979 Steady gravity–capillary waves on deep water-I. Weakly nonlinear waves. *Stud. Appl. Maths* **60**, 183–210.

Chen, B. & Saffman, P. G. 1980 Steady gravity–capillary waves on deep water-II. Numerical results for finite amplitude. *Stud. Appl. Maths* **62**, 95–111.

Clift, R., Grace, J. R. & Weber, M. E. 1978 *Bubbles, Drops, and Particles.* Academic Press.

Dandy, D. S. & Leal, L. G. 1986 Boundary layer separation from a smooth slip surface. *Phys. Fluids* **29**, 1360–1366.

Dandy, D. S. & Leal, L. G. 1989 Buoyancy-driven motion of a deformable drop through a quiescent liquid at intermediate Reynolds numbers. *J. Fluid Mech.* **208**, 161–192.

El Sawi, M. 1974 Distorted gas bubbles at large Reynolds number. *J. Fluid Mech.* **62**, 163–183.

Harper, J. F. 1972 Motion of bubbles and drops through liquids. *Adv. Appl. Mech.* **12**, 59–129.

Harper, J. F. 1982 Surface activity and bubble motion. *Appl. Sci. Res.* **38**, 343–352.

Harper, J. F. & Moore, D. W. 1968 The motion of a spherical liquid drop at high Reynolds number. *J. Fluid Mech.* **32**, 367–391.

Lamb, H. 1932 *Hydrodynamics.* Dover.

Miksis, M., Vanden-Broeck, J.-M. & Keller, J. B. 1981 Axisymmetric bubble or drop in a uniform flow. *J. Fluid Mech.* **108**, 89–100.

Miksis, M., Vanden-Broeck, J.-M. & Keller, J. B. 1982 Rising bubbles. *J. Fluid Mech.* **123**, 31–41.

Moffatt, H. K. & Moore, D. W. 1978 The response of Hill's spherical vortex to a small axisymmetric disturbance. *J. Fluid Mech.* **87**, 749–760.

Moore, D. W. 1959 The rise of a gas bubble in a viscous fluid. *J. Fluid Mech.* **6**, 113–130.

Moore, D. W. 1963 The boundary layer on a spherical gas bubble. *J. Fluid Mech.* **16**, 161–176.

Moore, D. W. 1965 The velocity of rise of distorted gas bubbles in a liquid of small viscosity. *J. Fluid Mech.* **23**, 749–766.

Moore, D. W., Saffman, P. G. & Tanveer, S. 1988 The calculation of some Batchelor flows: the Sadovskii vortex and rotational corner flow. *Phys. Fluids* **31**, 978–990.

Oliver, D. L. R. & Chung, J. N. 1987 Flow about a fluid sphere at low to moderate Reynolds numbers. *J. Fluid Mech.* **177**, 1–18.

Pozrikidis, C. 1986 The nonlinear instability of Hill's vortex. *J. Fluid Mech.* **168**, 337–367.

Rivkind, V. Y. & Ryskin, G. M. 1976 Flow structure in motion of a spherical drop in a fluid medium at intermediate Reynolds numbers. *Fluid Dyn.* **1**, 8–15.

Ryskin, G. & Leal, L. G. 1984 Numerical solution of free-boundary problems in fluid mechanics. Part 2. Buoyancy-driven motion of a gas bubble through a quiescent liquid. *J. Fluid Mech.* **148**, 19–35.

Winnikow, S. & Chao, B. T. 1966 Droplet motion in purified systems. *Phys. Fluids* **9**, 50–61.